Generalized finite element method for modeling nearly incompressible bimaterial hyperelastic solids

K.R. Srinivasan [a], K. Matouš [a,b,*], P.H. Geubelle [a]

[a] Department of Aerospace Engineering, University of Illinois at Urbana-Champaign, 104 South Wright Street, Urbana, IL 61801, USA
[b] Computational Science and Engineering, University of Illinois at Urbana-Champaign, 1304 West Springfield Avenue, Urbana, IL 61801, USA

ABSTRACT

An extension of the generalized finite element method to the class of mixed finite element methods is presented to tackle heterogeneous systems with nearly incompressible non-linear hyperelastic material behavior. In particular, heterogeneous systems with large modulus mismatch across the material interface undergoing large strains are investigated using two formulations, one based on a continuous deformation map, the other on a discontinuous one. A bimaterial patch test is formulated to assess the ability of the two formulations to reproduce constant stress fields, while a mesh convergence study is used to examine the consistency of the formulations. Finally, compression of a model heterogeneous propellant pack is simulated to demonstrate the robustness of the proposed discontinuous deformation map formulation.

© 2008 Elsevier B.V. All rights reserved.

1. Introduction

The numerical treatment of reinforced rubbery materials such as tires and energetic materials poses two key challenges. The first one is the accurate representation and discretization of the heterogeneous microstructure, especially for composite materials with high reinforcement volume fraction such as those found in solid propellants and explosives (see Fig. 1). The second challenge is associated with the markedly disparate material response of the constituent phases, which usually consist of very stiff particles embedded in a highly compliant nearly incompressible matrix that often experiences large deformations.

A relatively recent addition to the set of numerical tools, the generalized finite element method (GFEM) [14,35,6,28], which allows for the construction of elements that do not conform to the microstructure, is increasingly considered as an attractive way to tackle the computational geometry challenge. This technique has been used with some success in the treatment of bimaterial interfaces. For example, Moës et al. [27] have used a partition of unity-based extended finite element method that permits intra-element discontinuities by enriching the finite element approximation with a *ridge* function. The extended finite element method has also been applied to debonding of interfaces by Hettich and Ramm [19], who

used the *ridge* function in conjunction with a *Heaviside* function and a traction–separation law. Methods of the discontinuous Galerkin type include the work of Hansbo and Hansbo [18] and Mergheim and Steinmann [26], where the Nitsche method is used to balance the fluxes across the intra-element bimaterial discontinuity.

In addition to the complex heterogeneous microstructure, as shown in Fig. 1, the second challenge associated with the modeling of energetic materials arises from significant differences in material responses of particles and a matrix, caused in part by the nearly incompressible non-linear material behavior of the matrix. Traditionally, incompressibility is enforced using a class of mixed finite element methods [32], where the finite element interpolant spaces for displacement and pressure are subject to the Babuška–Brezzi conditions [8]. In order to satisfy the Babuška–Brezzi conditions, higher-order interpolations for displacements and lower-order interpolations for pressure (e.g., P_2/P_1 element) are required. However, the advent of stabilized formulations [20] provide means to use lower-order interpolations for both fields (e.g., P_1/P_1 element) and have been applied successfully to model linear elasticity [24], hyperelasticity [1], elasto-plasticity [31], and particle–matrix debonding in particle-reinforced elastomers [25].

The ability of the GFEM to handle bimaterial problems under plane strain with vastly different properties both in terms of modulus mismatch (with particle-to-matrix shear modulus ratios in excess of 1000) and the isochoric nature of the deformation is still to be investigated and is the focus of the present work. The treatment of incompressibility within the context of non-linear
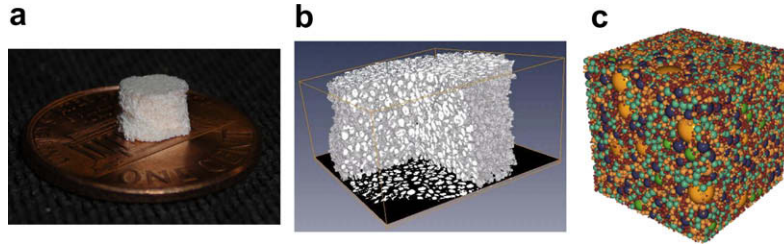
Fig. 1. Heterogeneous solid propellant; (a) a sample of the heterogeneous solid propellant [11]; (b) a tomographic image of the complex microstructure of the oxidizer particles embedded in the polymeric binder (fuel) [11]; (c) computer generated pack used in numerical modeling [22].

kinematics and the GFEM has been primarily devoted to fracture in a homogeneous material [13,23]. It appears that the only other work which addresses incompressibility using the GFEM under plane strain conditions is based on a geometrically non-linear assumed strain method developed by Dolbow and Devan [13], where coarse mesh accuracy and mesh locking problems in the fracture of compressible and nearly incompressible homogeneous materials were examined. Legrain et al. [23] studied the fracture in rubber-like materials under plane stress conditions using suitable crack tip enrichments. In that work, however, plane stress conditions facilitated the explicit evaluation of the hydrostatic pressure and a standard displacement-based finite element method sufficed.

The objective of the present work is to develop a numerical framework, based on the generalized finite element method, capable of simulating heterogeneous materials that exhibit nearly incompressible material behavior and high modulus mismatch ratios across a material interface. In this paper, we present two formulations, a continuous deformation map (CDM) based on the *ridge* enrichment, and a discontinuous deformation map (DDM) based on a combination of the *Heaviside* enrichment with Lagrange multipliers. This combination has previously been utilized by Belytschko et al. [7] to study discontinuities in tangential displacements across interface cracks, by Vaughan et al. [38] to study singular sources and discontinuous coefficients in scalar elliptic equations and by Kim et al. [21] to impose frictional contact constraints on intra-element or embedded surfaces, albeit for small deformations with linear elastic material behavior. The present work describes and compares the CDM and DDM formulations used to model the motion of a bimaterial nearly incompressible hyperelastic solid undergoing large deformations, with the generalized finite element formulation presented as an extension of the classical mixed finite element method. In particular, the effect of material modulus mismatch across the bimaterial interface using low-order Q_1/P_0 elements is highlighted.

The remainder of the paper is organized as follows. In Section 2, the governing equations for the motion of a hyperelastic bimaterial body are summarized, followed in Section 3 by the derivation of a variational formulation in the context of a continuous and a discontinuous map. The generalized finite element approximations, in the context of a mixed method, are derived in Section 4. Section 5 describes the patch and convergence tests employed to assess the numerical methodology under high modulus mismatches, and an example is presented to demonstrate the efficacy of the method. In this paper, we denote second-order tensors with uppercase boldface Roman letters, e.g., **F**, while vectors are denoted by boldface italic Roman and Greek letters, e.g., **u** and **λ**, and fourth-order tensors are denoted using the calligraphic font, e.g., $\mathscr{A}$. Finally, the trace of a second-order tensor **A** is given by tr(**A**).

2. Governing equations

Consider a hyperelastic body, as shown in Fig. 2, in an initial configuration $\mathscr{B}_0 \subset \mathbb{R}^3$ that undergoes the motion $\phi(\mathbf{X}, t)$ to the
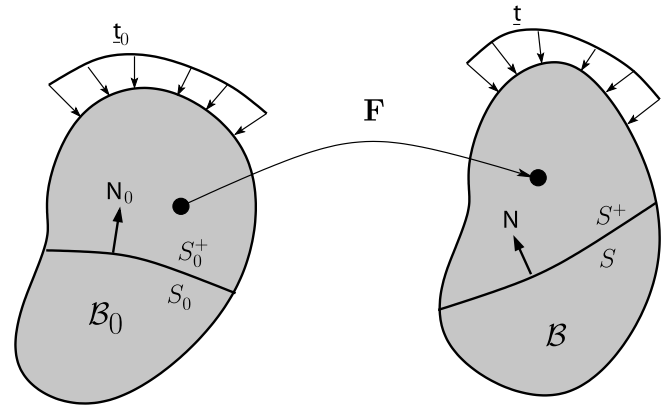

Fig. 2. Illustration of the mapping of a bimaterial system from $\mathscr{B}_0$ to $\mathscr{B}$.

current configuration $\mathscr{B} \subset \mathbb{R}^3$. Let $\mathbf{F}(\mathbf{X}, t) = \nabla \phi(\mathbf{X}, t)$ be the deformation at the current time $t \in \mathbb{R}^+$ with the Jacobian given by $J = \det(\mathbf{F})$. Here $\mathbf{X}$ and $\mathbf{x}$ $(\in \mathbb{R}^3)$ designate the position of a particle in the reference $\mathscr{B}_0$ and current $\mathscr{B}$ configuration, respectively. The displacement vector $\mathbf{u}$ is obtained from $\mathbf{x} = \mathbf{X} + \mathbf{u}$.

Suppose now that the body is divided by a material interface S_0 with a unit normal $\mathbf{N}_0$. For the sake of simplicity, we assume that the material interface partitions the body into two subbodies $\mathscr{B}_0^\pm$, occupying the plus and minus sides of the material interface, $S_0^\pm$, respectively. The deformation on either side of the interface is denoted by $\phi^\pm : \mathscr{B}_0^\pm \to \mathscr{B}^\pm$. The governing equations in the reference configuration are given by

$$
\begin{aligned}
\nabla \cdot \mathbf{P} + \mathbf{b}_0 &= 0 \quad \text{in } \mathscr{B}_0^\pm, \\
\mathbf{P} \cdot \mathbf{N}_0 &= \underline{\mathbf{t}}_0 \quad \text{on } \partial \mathscr{B}_T, \\
[\![\mathbf{P} \cdot \mathbf{N}_0]\!] &= 0 \quad \text{on } S_0^\pm, \\
\phi &= \phi_p \text{ on } \partial \mathscr{B}_u,
\end{aligned}
\tag{1}
$$

where $[\![\cdot]\!]$ is the jump operator, **P** is the first Piola-Kirchhoff stress, $\mathbf{b}_0$ is the body force vector acting per unit volume of $\mathscr{B}_0^\pm$, $\underline{\mathbf{t}}_0$ is the externally applied traction vector on $\partial \mathscr{B}_T$ and ϕ_p is the externally applied displacement vector on $\partial \mathscr{B}_u$, with $\partial \mathscr{B}_T \cap \partial \mathscr{B}_u = \emptyset$.

For nearly incompressible materials, the significant difference in material shear and bulk response is handled through a multiplicative decomposition of the deformation gradient into a dilational/volumetric part and a deviatoric/isochoric part. The volume-preserving part of the deformation gradient **F** is given by

$$
\widehat{\mathbf{F}} = J^{-\frac{1}{3}} \mathbf{F},
\tag{2}
$$

while an independent variable θ is used to capture the volumetric response

$$
\theta = J,
\tag{3}
$$

and we introduce $\overline{\mathbf{F}} = \theta^{\frac{1}{3}} \widehat{\mathbf{F}}$ as a mixed deformation gradient. Note that, in the finite element formulation that follows, (3) is enforced in a weak sense.

To close the system of equations in (1), we assume the material behavior of the bulk to be hyperelastic and nearly incompressible. The strain energy function W is composed of distortional $\widehat{W}$ and dilatational U parts [32],

$$W(\theta^{\frac{1}{3}}\widehat{\mathbf{F}}) = \widehat{W}(\mathbf{F}) + U(\theta), \tag{4}$$

and the standard nearly incompressible Neo-Hookean material model is employed

$$\widehat{W}(\mathbf{F}) = \frac{1}{2}\mu\left[J^{-\frac{2}{3}}\mathrm{tr}(\mathbf{F}^T\mathbf{F}) - 3\right],$$
$$U(\theta) = \frac{1}{2}\kappa(\theta - 1)^2. \tag{5}$$

Here, μ is the shear modulus and κ is the bulk modulus of the incompressible material. The hyperelastic constitutive equation reads

$$\mathbf{P} = \frac{\partial\widehat{W}(\mathbf{F})}{\partial\mathbf{F}}\bigg|_{\mathbf{F}=\bar{\mathbf{F}}} + \underbrace{\frac{\mathrm{d}U}{\mathrm{d}\theta}}_{p}\frac{\partial\theta}{\partial\mathbf{F}}\bigg|_{\mathbf{F}=\bar{\mathbf{F}}}, \tag{6}$$

where p is the hydrostatic pressure.

3. Variational formulation

For completeness and clarity of presentation, we summarize the variational formulations for two approaches used in this work to describe the motions $\phi^{\pm}$. The first approach is based on methods that ensure continuity in deformation maps of $\phi^{\pm}$ but allow for jumps in the deformation gradients $\mathbf{F}^{\pm} = \nabla\phi^{\pm}$. The second approach admits jumps in deformation maps as well as its gradients, with the continuity of the deformation maps enforced weakly.

3.1. Continuous deformation map (CDM)

The motion of subbodies $\mathscr{B}_0^{\pm}$ is restricted along the interface S_0 to ensure continuity of the deformation maps $\phi^{\pm}$. This restriction, combined with Eqs. (1)–(3), enables the formulation of a mixed three-field de Veubeke–Hu–Washizu variational statement [32] for the finite deformation bimaterial hyperelastic problem, with a Lagrange functional Π_{CDM} defined as

$$\Pi_{\mathrm{CDM}}(\phi, p, \theta) = \int_{\mathscr{B}_0^{\pm}}\{\underbrace{\widehat{W}(\mathbf{F}) + U(\theta)}_{W(\theta^{\frac{1}{3}}\widehat{\mathbf{F}})}\}\mathrm{d}V_0 + \int_{\mathscr{B}_0^{\pm}}p(J - \theta)\mathrm{d}V_0 + \Pi_{\mathrm{ext}}, \tag{7}$$

where p is the Lagrange multiplier, which corresponds for certain functions W to the pressure (Eq. (6)). Π_{ext} is the total potential energy associated with body forces $\boldsymbol{b}_0$ and externally applied tractions $\boldsymbol{t}_0$.

The stationarity of (7), from which the corresponding Euler–Lagrange equations are derived, leads to

$$\delta\Pi_{\mathrm{CDM}}(\phi, p, \theta) = \int_{\mathscr{B}_0^{\pm}}\widehat{\mathbf{P}} : \delta\mathbf{F}\,\mathrm{d}V_0 + \int_{\mathscr{B}_0^{\pm}}U'(\theta)\delta\theta\mathrm{d}V_0 + \int_{\mathscr{B}_0^{\pm}}\delta p(J - \theta)\mathrm{d}V_0$$
$$+ \int_{\mathscr{B}_0^{\pm}}p(\delta J - \delta\theta)\mathrm{d}V_0 + \delta\Pi_{\mathrm{ext}} = 0 \tag{8}$$

for all admissible variations

$$\delta\boldsymbol{u} \in [H^1(\mathscr{B}_0)], \quad \delta\boldsymbol{u} = \boldsymbol{0} \text{ on } \partial\mathscr{B}_{\boldsymbol{u}}, \quad \delta p \in L_2(\mathscr{B}_0),$$
$$\delta\theta \in L_2(\mathscr{B}_0), \tag{9}$$

where $H^1(\mathscr{B}_0)$ is the Sobolev space of square-integrable functions with weak derivatives up to first-order with range in $\mathbb{R}^3$, and $\widehat{\mathbf{P}} = \frac{\partial\widehat{W}(\mathbf{F})}{\partial\mathbf{F}}$.

A second variation of (7) is also needed to construct the consistent linearization of (8):

$$\Delta\delta\Pi_{\mathrm{CDM}}(\phi, p, \theta) = \int_{\mathscr{B}_0^{\pm}}\delta\mathbf{F} : \widehat{\mathscr{A}} : \Delta\mathbf{F}\,\mathrm{d}V_0 + \int_{\mathscr{B}_0^{\pm}}\delta\theta\,U''(\theta)\Delta\theta\mathrm{d}V_0$$
$$+ \int_{\mathscr{B}_0^{\pm}}\delta p(\Delta J - \Delta\theta)\mathrm{d}V_0 + \int_{\mathscr{B}_0^{\pm}}(\delta J - \delta\theta)\Delta p\,\mathrm{d}V_0$$
$$+ \int_{\mathscr{B}_0^{\pm}}p\Delta\delta J\mathrm{d}V_0 + \Delta\delta\Pi_{\mathrm{ext}}. \tag{10}$$

Here, $\widehat{\mathscr{A}} = \frac{\partial^2\widehat{W}}{\partial\mathbf{F}\partial\mathbf{F}}$ is the fourth-order material tangent pseudo-moduli, and the first and second variations of J are

$$\delta J = J\mathbf{F}^{-T} : \delta\mathbf{F},$$
$$\Delta\delta J = \delta\mathbf{F} : \underbrace{\{J(\mathbf{F}^{-T} \otimes \mathbf{F}^{-T}) + J\mathscr{T}(-\mathbf{F}^{-1} \boxtimes \mathbf{F}^{-T})\}}_{\widetilde{\mathscr{A}}} : \Delta\mathbf{F}, \tag{11}$$

where $\mathscr{T}$ is the fourth-order transposition tensor ($\mathscr{T}\mathbf{A} = \mathbf{A}^T$). The $\otimes$ and $\boxtimes$ tensor products of two second-order tensors $\mathbf{A}$ and $\mathbf{B}$ are defined as

$$(\mathbf{A} \otimes \mathbf{B})_{ijkl} = \mathbf{A}_{ij}\mathbf{B}_{kl},$$
$$(\mathbf{A} \boxtimes \mathbf{B})_{ijkl} = \mathbf{A}_{ik}\mathbf{B}_{jl}. \tag{12}$$

3.2. Discontinuous deformation map (DDM)

Suppose now that the motion of the subbodies $\mathscr{B}_0^{\pm}$ is not restricted along the interface S_0. Instead, the continuity of the deformation maps is enforced weakly using Lagrange multipliers λ. The modified de Veubeke–Hu–Washizu variational statement reads

$$\Pi_{\mathrm{DDM}}(\phi, p, \theta, \lambda) = \int_{\mathscr{B}_0^{\pm}}\{\widehat{W}(\mathbf{F}) + U(\theta)\}\mathrm{d}V_0 + \int_{\mathscr{B}_0^{\pm}}p(J - \theta)\mathrm{d}V_0$$
$$+ \int_{S_0}\lambda \cdot [\![\phi]\!]\mathrm{d}S_0 + \Pi_{\mathrm{ext}}. \tag{13}$$

In (13), an additional independent vector variable λ is introduced, which represents the Lagrange multipliers, i.e., the interface tractions.

The corresponding stationarity condition gives

$$\delta\Pi_{\mathrm{DDM}}(\phi, p, \theta, \lambda) = \int_{\mathscr{B}_0^{\pm}}\widehat{\mathbf{P}} : \delta\mathbf{F}\,\mathrm{d}V_0 + \int_{\mathscr{B}_0^{\pm}}U'(\theta)\delta\theta\,\mathrm{d}V_0$$
$$+ \int_{\mathscr{B}_0^{\pm}}\delta p(J - \theta)\mathrm{d}V_0 + \int_{\mathscr{B}_0^{\pm}}p(\delta J - \delta\theta)\mathrm{d}V_0$$
$$+ \int_{S_0}\delta\lambda \cdot [\![\phi]\!]\mathrm{d}S_0 + \int_{S_0}\lambda \cdot [\![\delta\phi]\!]\mathrm{d}S_0 + \delta\Pi_{\mathrm{ext}} = 0 \tag{14}$$

for all admissible variations (9) and $\delta\lambda \in \left[H^{-\frac{1}{2}}(S_0)\right]$. The second variations, similar to (10), are derived to obtain consistent tangents

$$\Delta\delta\Pi_{\mathrm{DDM}}(\phi, p, \theta, \lambda) = \int_{\mathscr{B}_0^{\pm}}\delta\mathbf{F} : \widehat{\mathscr{A}} : \Delta\mathbf{F}\,\mathrm{d}V_0 + \int_{\mathscr{B}_0^{\pm}}\delta\theta U''(\theta)\Delta\theta\mathrm{d}V_0$$
$$+ \int_{\mathscr{B}_0^{\pm}}\delta p(\Delta J - \Delta\theta)\mathrm{d}V_0 + \int_{\mathscr{B}_0^{\pm}}(\delta J - \delta\theta)\Delta p\,\mathrm{d}V_0$$
$$+ \int_{\mathscr{B}_0^{\pm}}p\Delta\delta J\mathrm{d}V_0 + \int_{S_0}\delta\lambda \cdot [\![\Delta\phi]\!]\mathrm{d}S_0$$
$$+ \int_{S_0}\Delta\lambda \cdot [\![\delta\phi]\!]\mathrm{d}S_0 + \Delta\delta\Pi_{\mathrm{ext}}. \tag{15}$$

4. Generalized finite element method

A *Partition of unity* method (PUM) is used to obtain a discrete representation of the three-field variational statements (7) and (13). The PUM developed by Babuška and Melenk [5] and the method of clouds proposed by Duarte and Oden [16] have the ability to incorporate *a priori* into the finite element space

the knowledge of the governing partial differential equations. Instances of the PUM, the generalized finite element method (GFEM) [15,33,17] and the extended finite element method (XFEM) [12,36] have achieved some success in solving partial differential equations with strong and weak discontinuities. This section extends the formulation to the case of near-incompressible materials under large deformations for the two variational statements described in the previous section, i.e., the continuous (7) and discontinuous (13) formulation.

4.1. Discretization

Let the domain $\mathscr{B}_0$ be divided into N^e elements $\mathscr{B}_0^e$, with the element edges chosen independently of the bimaterial interface S_0. The discretization is composed of N_J *displacement* nodes, with partition of unity shape functions χ used to describe the geometry and the coordinates in the reference configuration $\mathscr{B}_0$. Let ω_J be the support of any node $J \in N_J$. A set of enriched nodes N_I (Fig. 3a) is then defined as

$$N_I = \{J | J \in N_J, \omega_J \cap S_0 \neq \emptyset\}. \tag{16}$$

The approximate displacement field $\tilde{\boldsymbol{u}}$ is composed of a *coarse* displacement field $\tilde{\boldsymbol{u}}^s$ and a set of α enriched (*fine*) displacement fields $\tilde{\boldsymbol{u}}_\alpha^e$ as

$$\tilde{\boldsymbol{u}}(\boldsymbol{X}) = \underbrace{\sum_j^{N_J} \chi_j(\boldsymbol{X}) \hat{\boldsymbol{u}}_j}_{\tilde{\boldsymbol{u}}^s(\boldsymbol{X})} + \sum_\alpha \underbrace{\sum_i^{N_I} \chi_i(\boldsymbol{X}) \psi^\alpha \hat{\boldsymbol{a}}_i^\alpha}_{\tilde{\boldsymbol{u}}_\alpha^e(\boldsymbol{X})}, \tag{17}$$

where every node $I \in N_I$ is enriched with α linearly independent enrichment functions ψ^α, and $\hat{\boldsymbol{a}}_i^\alpha$ are the additional degrees of freedom introduced to approximate the *fine* enriched displacement field $\tilde{\boldsymbol{u}}_\alpha^e$. The choice of enrichment functions is strongly influenced by the desired regularity and behavior of solution $\tilde{\boldsymbol{u}}(\boldsymbol{X})$ around the vicinity of the interface S_0. Discussion on the choice of the enrichment functions is presented in Section 4.3.

The approximations to pressure p and volumetric field θ are constructed from partition of unity shape functions as well. The pressure nodes N_J^p and the volumetric nodes N_J^θ are enriched if their supports ω_J^p and ω_J^θ are intersected by the interface S_0, as shown in Fig. 3b:

$$N_I^p = \{n_I^p | n_I^p \in N_J^p, \omega_J^p \cap S_0 \neq \emptyset\},$$
$$N_I^\theta = \{n_I^\theta | n_I^\theta \in N_J^\theta, \omega_J^\theta \cap S_0 \neq \emptyset\}. \tag{18}$$

As in (17), approximations of pressure $\tilde{p}$ and volumetric field $\tilde{\theta}$ can be constructed as

$$\tilde{p}(\boldsymbol{X}) = \underbrace{\sum_j^{N^p} \chi_j^p(\boldsymbol{X}) \hat{p}_j}_{p^s(\boldsymbol{X})} + \sum_{\alpha^p} \underbrace{\sum_i^{N_I^p} \chi_i^p(\boldsymbol{X}) \psi^{\alpha^p} \hat{a}_i^{\alpha^p}}_{p_{\alpha^p}^e(\boldsymbol{X})},$$

$$\tilde{\theta}(\boldsymbol{X}) = \underbrace{\sum_j^{N^\theta} \chi_j^\theta(\boldsymbol{X}) \hat{\theta}_j}_{\theta^s(\boldsymbol{X})} + \sum_{\alpha^\theta} \underbrace{\sum_i^{N_I^\theta} \chi_i^\theta(\boldsymbol{X}) \psi^{\alpha^\theta} \hat{a}_i^{\alpha^\theta}}_{\theta_{\alpha^\theta}^e(\boldsymbol{X})}. \tag{19}$$

For the continuous deformation maps described in Section 3.1, substituting the approximations for $\boldsymbol{u}$, p, and θ in (8) and invoking arbitrariness of the variations $\delta(\cdot)$, the following system of non-linear Euler–Lagrange equations yields:

$$\mathscr{R}_{\boldsymbol{u}^s} = \int_{\mathscr{B}_0^\pm} \widehat{\mathbf{P}} : \delta \widetilde{\mathbf{F}}^s \, dV_0 + \int_{\mathscr{B}_0^\pm} \tilde{p} \widetilde{J} \widetilde{\mathbf{F}}^{-\mathrm{T}} : \delta \widetilde{\mathbf{F}}^s \, dV_0 = 0,$$

$$\mathscr{R}_{\boldsymbol{u}^e}^\alpha = \int_{\mathscr{B}_0^\pm} \widehat{\mathbf{P}} : \delta \widetilde{\mathbf{F}}_\alpha^e \, dV_0 + \int_{\mathscr{B}_0^\pm} \tilde{p} \widetilde{J} \widetilde{\mathbf{F}}^{-\mathrm{T}} : \delta \widetilde{\mathbf{F}}_\alpha^e \, dV_0 = 0,$$

$$\mathscr{R}_{p^s} = \int_{\mathscr{B}_0^\pm} (\widetilde{J} - \tilde{\theta}) \delta \tilde{p}^s \, dV_0 = 0,$$

$$\mathscr{R}_{p^e}^{\alpha^p} = \int_{\mathscr{B}_0^\pm} (\widetilde{J} - \tilde{\theta}) \delta \tilde{p}_{\alpha^p}^e \, dV_0 = 0, \tag{20}$$

$$\mathscr{R}_{\theta^s} = \int_{\mathscr{B}_0^\pm} (U'(\tilde{\theta}) - \tilde{p}) \delta \tilde{\theta}^s \, dV_0 = 0,$$

$$\mathscr{R}_{\theta^e}^{\alpha^\theta} = \int_{\mathscr{B}_0^\pm} (U'(\tilde{\theta}) - \tilde{p}) \delta \tilde{\theta}_{\alpha^\theta}^e \, dV_0 = 0,$$

where the admissible variations $\delta(\cdot)$ are described in Appendix A.

In the case of a discontinuous deformation map (Section 3.2), the Lagrange multiplier $\boldsymbol{\lambda}$ introduced in (13) can be viewed as a Dirac-Delta distribution centered around the interface. Therefore, it is sufficient to discretize the interface S_0 for constructing approximations $\tilde{\boldsymbol{\lambda}}$. The discretization, illustrated in Fig. 4, enables construction of the approximate vector field $\tilde{\boldsymbol{\lambda}}$ as

$$\tilde{\boldsymbol{\lambda}}(\boldsymbol{X}) = \sum_{j=1}^{N^\lambda} \chi_j^\lambda(\boldsymbol{X}) \hat{\boldsymbol{\lambda}}_j, \tag{21}$$

where N^λ is the set of Lagrange multiplier nodes in the discretization. It should be noted that the choice of basis functions χ, χ^p, χ^θ, and χ^λ is subject to the inf–sup conditions ($\inf_{\boldsymbol{u}} \inf_\theta \sup_p \sup_\lambda \Pi_{\mathrm{DDM}}(\boldsymbol{u}, \theta, p, \lambda)$) for the method to be unconditionally convergent and stable [8,3,4]. Since we focus on the Q_1/P_0
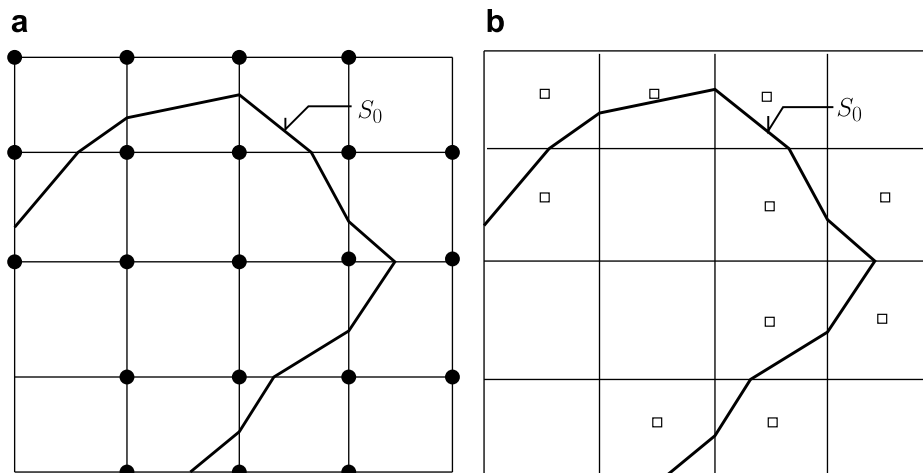

Fig. 3. Section of the finite element mesh in the vicinity of the material interface S_0 showing (a) the enriched displacement nodes for a bilinear Q_1 element; (b) the enriched pressure/volumetric nodes at element centers for a piecewise constant pressure/volume P_0 element.
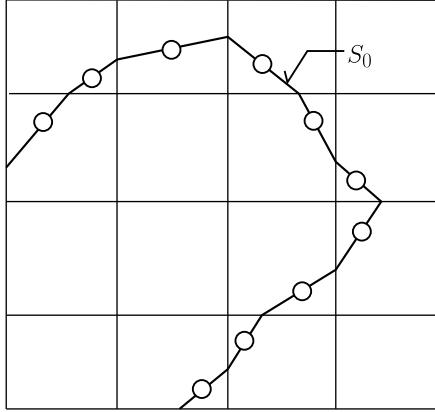
Fig. 4. Section of the finite element mesh showing the discretization of the interface for the approximation of the Lagrange multiplier vector field λ.

element, that does not satisfy the inf–sup conditions on u and p, we assess the element through the patch test.

Correspondingly, a system of non-linear Euler–Lagrange equations, similar to (20), is obtained as

$$
\begin{aligned}
\mathscr{R}_{u^s} &= \int_{\mathscr{B}_0^{\pm}} \widehat{\mathbf{P}} : \delta\widetilde{\mathbf{F}}^s \, dV_0 + \int_{\mathscr{B}_0^{\pm}} \tilde{p}\widetilde{J}\widetilde{\mathbf{F}}^{-T} : \delta\widetilde{\mathbf{F}}^s \, dV_0 \\
&\quad + \int_{S_0} \tilde{\lambda} \cdot [\![\delta\tilde{u}^s]\!] \, dS_0 = 0, \\
\mathscr{R}_{u^e}^{\alpha} &= \int_{\mathscr{B}_0^{\pm}} \widehat{\mathbf{P}} : \delta\widetilde{\mathbf{F}}_{\alpha}^e \, dV_0 + \int_{\mathscr{B}_0^{\pm}} \tilde{p}\widetilde{J}\widetilde{\mathbf{F}}^{-T} : \delta\widetilde{\mathbf{F}}_{\alpha}^e \, dV_0 \\
&\quad + \int_{S_0} \tilde{\lambda} \cdot [\![\delta\tilde{u}_{\alpha}^e]\!] \, dS_0 = 0, \\
\mathscr{R}_{\lambda} &= \int_{S_0} \delta\tilde{\lambda} \cdot [\![\tilde{u}^s + \tilde{u}_{\alpha}^e]\!] \, dS_0 = 0.
\end{aligned}
\tag{22}
$$

The Euler–Lagrange equations for pressure (p^s, p^e) and the volume (θ^s, θ^e) fields are identical to those in (20) and therefore not repeated in (22). In order to obtain optimally convergent Newton–Raphson schemes, consistent linearization of the residual Eqs. (20) and (22) is performed using the consistent tangent moduli derived in (10) and (15), respectively.

4.2. Geometry description and numerical integration

Let us describe the bimaterial interface as a zero level set of a functions $\Phi(X)$ approximated using the standard basis functions χ as

$$
\Phi(X) = \sum_{N_J} \chi_J \widehat{\Phi}(X_J).
\tag{23}
$$

In the above equation, the nodal level set function $\widehat{\Phi}$ is constructed at every node J as

$$
\widehat{\Phi}(X_J) = \text{sign}((X_J - X_I) \cdot N_0) \, \min(\|X_J - X_I\|),
\tag{24}
$$

where X_I denotes any point on the interface S_0, and N_0 is the outward pointing normal at X_I. As a result, each node in the finite element mesh stores an additional scalar $\widehat{\Phi}$, which is then used to track/detect the existence of an interface. Level sets are traditionally used to track moving fronts [30] and have been successfully used to model crack propagation [34,10,37], with the level set function updated every time step. In the present study, since stationary interfaces are considered, the level set function $\Phi(X)$ is computed at the outset and remains unchanged thereafter. For each node, the sign of the level set function Φ is used to check its position in $\mathscr{B}_0^+$, $\mathscr{B}_0^-$ or S_0. Similarly, elements are assigned to $\mathscr{B}_0^+$, $\mathscr{B}_0^-$ or an

intersected element set that contain a interface S_0. Implementation details on detection of the interface can be found in [36].

Conventional Gaussian quadrature is used to integrate the volume integrals in elements that lie completely in $\mathscr{B}_0^+$ or $\mathscr{B}_0^-$. Additional care is taken to compute the integrals in elements intersected by an interface. Moës et al. [29] proposed the partition of the intersected elements into triangles to perform accurate integrations. The same approach is adopted here and the elements are triangulated on either side of the interface with four Gaussian quadrature integration points. Tests have shown that the seven-point Gauss quadrature rule yield identical results. As indicated in [29], the triangulation resulting from the partition of the element is stored for integration purposes only, and no new nodes/elements are added to the existing finite element mesh.

4.3. Enrichment functions

To model weak discontinuities in bimaterial interfaces, Moës et al. [27] proposed a *ridge* function given by

$$
\psi(X) = \sum_i \chi_i(X)|\widehat{\Phi}(X_i)| - \left| \sum_i \chi_i(X)\widehat{\Phi}(X_i) \right|.
\tag{25}
$$

The *ridge* function is continuous across the interface S_0, though the gradients of the *ridge* function are discontinuous. The *ridge* enrichment is well suited for the method described in Section 3.1, and Moës et al. [27] reported optimally convergent results in the small strain regime for linear elastic materials with relatively small modulus mismatch. In this study, the convergence rates obtained through the *ridge* enrichment is further examined for large deformations of nearly incompressible materials with large modulus mismatch. Fig. 5a illustrates the nodal *ridge* enrichment function on a patch of elements bisected by a material interface.

In the case of discontinuous deformation maps (Section 3.2), the enrichment function ψ needs to be discontinuous. A simple choice for a discontinuous enrichment function is the *Heaviside* function [7,21], illustrated in Fig. 5b, defined as

$$
\psi(X) = \mathscr{H}(X) = \begin{cases} 1 & \text{if } \Phi(X) > 0, \\ 0 & \text{if } \Phi(X) < 0. \end{cases}
\tag{26}
$$

An alternate approach to Heaviside enrichments, is to discretize (14) using the Unfitted finite element method (UFEM) [18,26], where the intersected element is duplicated to represent the maps $\phi^{\pm}$ independently. A note on the equivalence of the GFEM/XFEM and UFEM is given in [2].

5. Numerical examples

In this section, patch and convergence tests are performed to assess the performance of the numerical methodologies developed in Section 3. The finite elements considered for the studies are the classical Q_1/P_0 element, a low-order element prevalently used in engineering simulations. The *Heaviside* function (26) is used as an enrichment for the pressure and volume fields in (19). A low-order piecewise constant approximation for the Lagrange multiplier is adopted as well.

5.1. Bimaterial patch test

A bimaterial patch test is devised to assess the capability of the numerical methods described in Section 4 to reproduce constant stress fields. Based on enrichment functions chosen in Section 4.3, the finite element approximation contains the space of piecewise linear displacement fields, and is therefore expected to reproduce constant stress fields exactly. The bimaterial patch test is composed of two nearly incompressible materials ($\kappa_1 = 1.25 \times 10^4$ MPa,
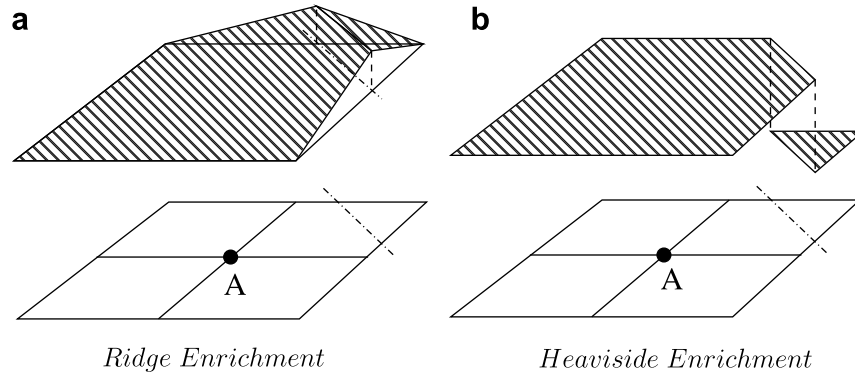
Fig. 5. Schematic of the support of node A bisected by a bimaterial interface with a (a) *ridge* enrichment; (b) Heaviside enrichment.

$\mu_1 = 2.5$ MPa, i.e., Poisson's ratio $\nu_1 = 0.4999$, and $\kappa_2 = 1.25 \times 10^7$ MPa, $\mu_2 = 2.5 \times 10^3$ MPa, i.e., Poisson's ratio $\nu_2 = 0.4999$), shown in Fig. 6, occupying the top and bottom halves of a square domain ($[-1\ 1] \times [-1\ 1]$) (units in mm). The bottom surface ($y = -1$) is restricted along the y-axis and free to move along the x-axis, while the left surface ($x = -1$) is restricted along the x-axis and free to move along the y-axis. A uniform displacement of $u_x = 0.05$ mm is applied to the surface on the right ($x = 1$), while the top surface ($y = 1$) is traction-free. The bimaterial patch test is solved on a straight mesh and a skewed mesh (Fig. 6) under plane strain conditions to study the effect of mesh orientation with respect to the material interface.

Fig. 7 depicts the spatial distribution of the pressure variable p in the bimaterial system for the straight and skewed mesh orientations. The use of the continuous deformation map formulation with the *ridge* enrichment function (25) is found to cause large oscillations ($\sim$25%) near the material interface in the skewed mesh orientation, as shown in Fig. 7b. The discontinuous deformation map formulation with the *Heaviside* enrichment and Lagrange multipliers is found to yield more accurate results, with oscillations near the interface (Fig. 7c and d) less than 0.1%. Similar small oscillations were observed in a discontinuous patch test devised by Dolbow and Devan [13], where an enriched assumed strain method is used to enforce the incompressibility constraint.

5.2. Convergence tests

We now turn our attention to a mesh convergence study for the numerical methods discussed in Sections 3.1 and 3.2. That study is performed on a square domain of length $L = 2$ mm (the *matrix*), filled with a circular inclusion (the *particle*) of radius $a = 0.4$ mm under a compressive load of 2 MPa carried out using Q_1/P_0 elements under 2-D plane strain conditions. Details of the loading and boundary conditions can be found in Fig. 8a. A level set function (24) is used to describe the circular inclusion, where the level set function is positive outside the circular inclusion and negative inside. The convergence study is carried out on structured uniform grids composed of $10 \times 10, 20 \times 20, 40 \times 40$, and 80×80 elements. A typical mesh for the bimaterial problem is shown in Fig. 8b. The error $\mathscr{E}_{\boldsymbol{u}}$ in displacement is defined using the H^1 Sobolev norm

$$\mathscr{E}_{\boldsymbol{u}} = \|\tilde{\boldsymbol{u}} - \boldsymbol{u}_{\mathrm{ref}}\|_{H^1} = \sqrt{\|\tilde{\boldsymbol{u}} - \boldsymbol{u}_{\mathrm{ref}}\|^2 + \|\nabla\tilde{\boldsymbol{u}} - \nabla\boldsymbol{u}_{\mathrm{ref}}\|^2}, \tag{27}$$

while the error measure $\mathscr{E}_p$ for the pressure field is defined as

$$\mathscr{E}_p = \|\tilde{p} - p_{\mathrm{ref}}\|_{L_2}. \tag{28}$$

Due to the absence of an analytical solution for the non-linear problem discussed here, a *fine* finite element mesh composed of 18 570 Q_1/P_0 elements and 18 841 nodes that conforms to the bimaterial interface is used as the reference solution in (27) and (28). The hyperelastic constitutive relations described in Section 2 are used to describe the material response of the matrix and the particle. The bulk and shear modulus of the matrix are $\kappa_m = 1.25 \times 10^4$ MPa and $\mu_m = 2.5$ MPa, while the material properties of the particle are varied to study the effect of the modulus mismatches, quantified by

$$\kappa^* = \frac{\kappa_p}{\kappa_m}, \quad \mu^* = \frac{\mu_p}{\mu_m}. \tag{29}$$
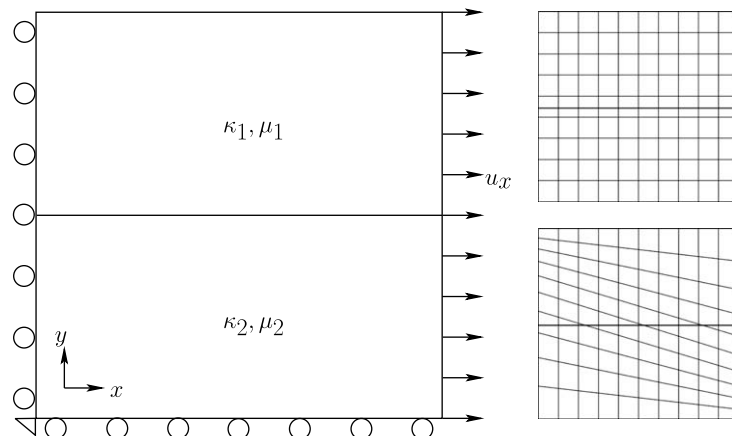

Fig. 6. Schematic of the bimaterial patch test problem with applied displacements u_x to the right surface. The patch test is performed on straight and skewed mesh orientations, shown on the right, where the bimaterial interface is independent of element edges.
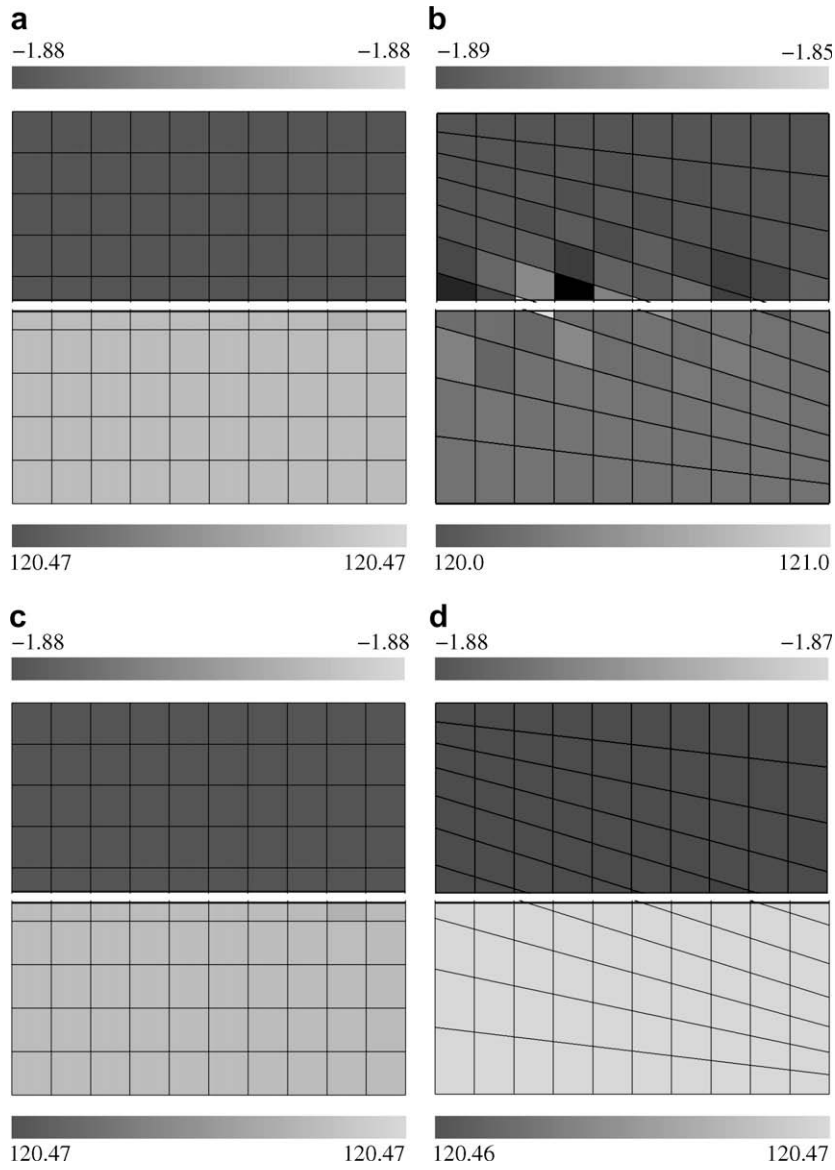
Fig. 7. Spatial distribution of the pressure variable *p* on each side of the bimaterial interface in the bimaterial patch test on (a) a straight mesh and (b) a skewed mesh with the *ridge* enrichment; (c) a straight mesh and (d) a skewed mesh with the *Heaviside* enrichment and Lagrange multipliers. Note that, the pressure *p* in each material domain is associated with its own grayscale legend to highlight the pressure instabilities.
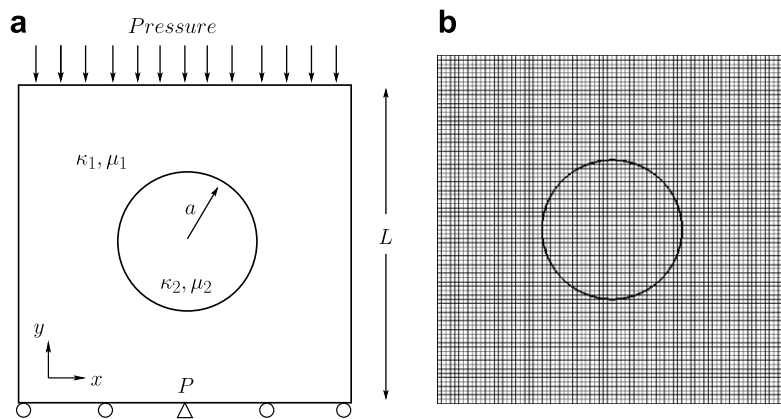

Fig. 8. (a) Schematic of the boundary value problem used for mesh convergence tests and (b) a sample 80×80 finite element mesh with an embedded inclusion.

Two sets of modulus mismatches are chosen, $(\kappa^*, \mu^*) = (10, 10)$ and $(\kappa^*, \mu^*) = (1000, 1000)$, to represent a moderate and a large mismatch.

Fig. 9 reports results for the two sets of moduli mismatches mentioned above. Fig. 9a shows the dependence of $\mathscr{E}_u$ on the mesh size h. It is observed that for a moderate mismatch, the convergence rates for the CDM and DDM formulations are near-optimal (Optimal rate = 1), and the accuracies of the two formulations are comparable. However, significant differences in accuracy are observed for a large mismatch, where the DDM formulation clearly outperforms the CDM one. The reason for higher accuracy is more evident from Fig. 9b that reports error in pressure $\mathscr{E}_p$. As observed for $\mathscr{E}_u$, the error in pressure $\mathscr{E}_p$ also indicates optimal convergence and comparable accuracies for the moderate modulus mismatch case in both formulations. However, striking differences appear for the large mismatch case, where the DDM formulation exhibits optimal convergence, while the CDM formulation appears to be *non-convergent*.

Fig. 10 shows the spatial convergence of the magnitude of the Lagrange multiplier solution plotted along the circumference of

Fig. 10. Distribution of the magnitude of the Lagrange multiplier along the circumference of the inclusion parameterized by polar angle $\varphi(-\pi, +\pi)$ for varying mesh sizes.

the inclusion. It is observed that the Lagrange multiplier field converges with mesh size h, albeit exhibiting some oscillatory behavior. These oscillations occur in portions of the Lagrange multiplier mesh that have very small support, i.e., where the interfacial mesh is very small compared to the bulk mesh size. The numerical method presented in this work leads to non-uniform Lagrange multiplier interface meshes and hence the traditional convergence tests for the Lagrange multiplier filed is not performed.

The spatial distribution of pressure p for the cases mentioned above is shown in Fig. 11. Fig. 11a and c depicts the pressure distribution in the bimaterial system for the moderate mismatch case and show smooth continuous pressure distributions within each material domain. For the large mismatch case (Fig. 11b and d), the pressure remains smooth for the DDM formulation, while a severe checkerboard type pattern is obtained for the CDM formulation. It is emphasized that the classical Q_1/P_0 element, though highly effective in practice, does not satisfy the Babuška–Brezzi condition on $\boldsymbol{u}$ and p [8]. It is likely that, for the CDM formulation with ridge enrichments, the observed checkerboard pattern is a manifestation of the aforementioned violation of the Babuška–Brezzi condition, although rigorous inf–sup tests would be required for a complete assessment [9]. As described in Section 3.1, the CDM formulation enriched with the ridge function, enforces the continuity of the deformation maps ($\phi^\pm$) strongly, and as a result, lower-order elements tend to lock causing spurious oscillations in the pressure field. The weak treatment of this continuity condition through Lagrange multipliers appears to alleviate the locking problem in the low-order element.

Beyond the stability of the pressure field, another advantage of using the DDM formulation with Lagrange multipliers is the ease of computing interfacial tractions. An accurate description of the spatial distribution of tractions along a bimaterial interface is of paramount importance for the simulation of debonding between the binder and particles [25]. The DDM formulation enables the automatic extraction of the interface traction fields obtained directly form the unknown solution vector λ. In Fig. 12, the normal traction λ_n along the bimaterial interface is shown, with the length of the arrows indicating their magnitude. For a compressive pressure load applied along the top surface, the inclusion/particle predominantly encounters compressive tractions at A and B, while experiencing a small amount of tensile tractions at C and D locations. It is

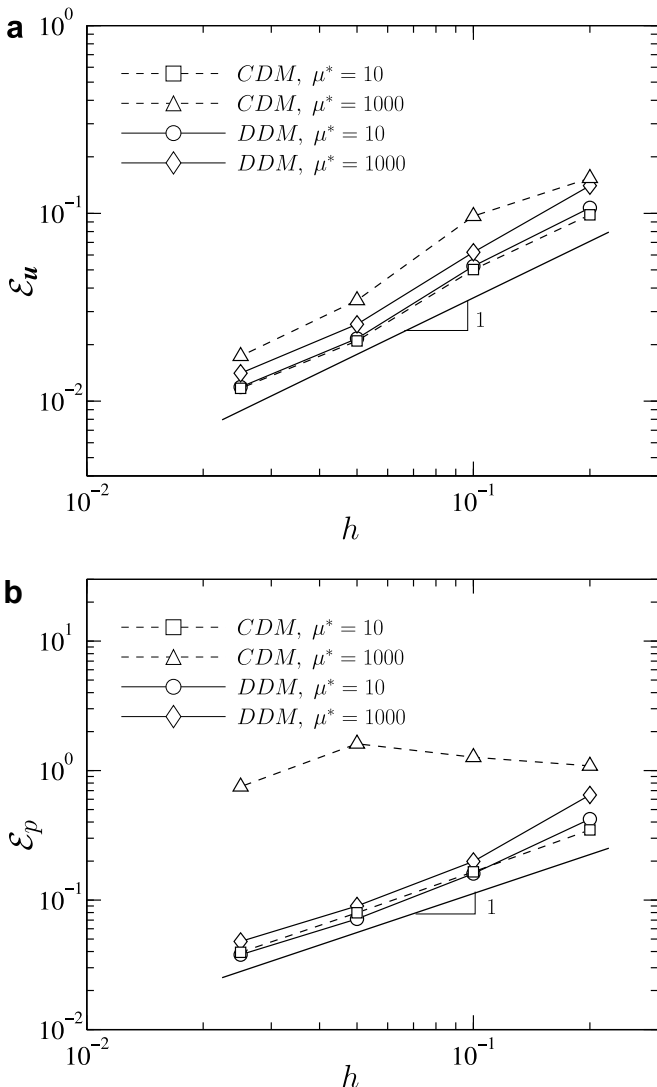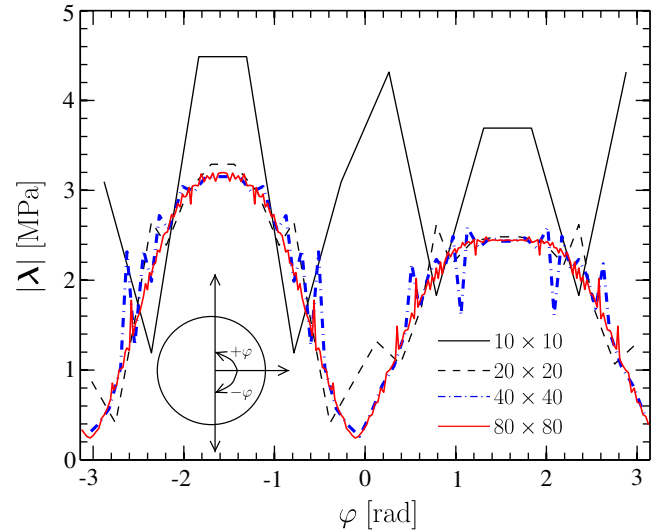**Fig. 9.** Log–log plots for the continuous deformation map (CDM) and the discontinuous deformation map (DDM) cases with varying modulus mismatches μ^* showing (a) the displacement error norm $\mathscr{E}_u$ as a function of the mesh size h; (b) the pressure error norm $\mathscr{E}_p$ as a function of the mesh size h.

a

| −2.79 | −1.82 | −0.82 | 0.11 |

b

| −3.18 | −1.97 | −0.76 | 0.44 |

c

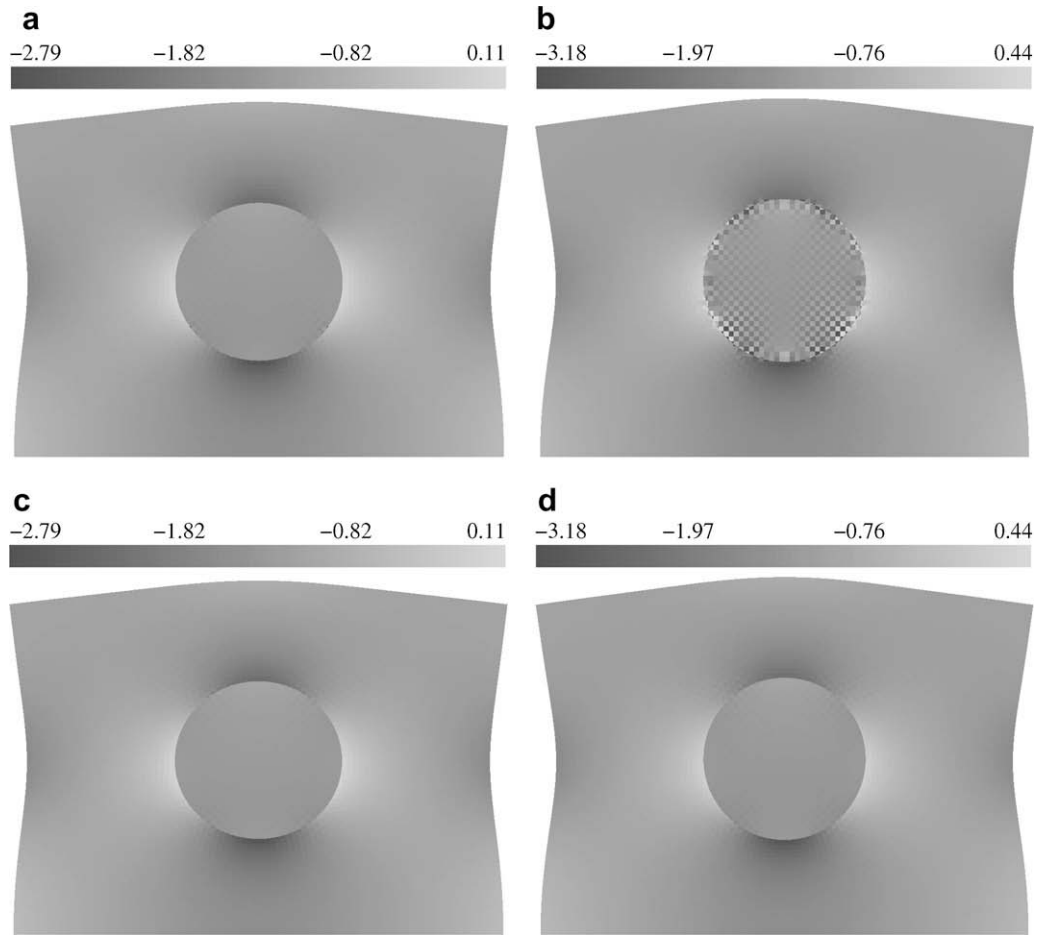| −2.79 | −1.82 | −0.82 | 0.11 |

d

| −3.18 | −1.97 | −0.76 | 0.44 |

Fig. 11. Spatial distribution of the pressure variable p for the continuous deformation map (CDM) with (a) $\mu^* = 10$; (b) $\mu^* = 1000$; and the discontinuous deformation map (DDM) with (c) $\mu^* = 10$; (d) $\mu^* = 1000$.

also observed that the normal traction field does not exhibit spurious oscillations along the interface. It is noted, however, that the computational expense associated with the DDM formulation increases with the number of discretization nodes on the interface.

Fig. 12. Spatial distribution of the normal tractions λ_n acting on the circular inclusion of the bimaterial test problem using the DDM formulation. Length of the arrows indicate the magnitude. All values in MPa.

5.3. Model heterogeneous propellant pack

To demonstrate the robustness of the DDM formulation, we now turn our attention to the particulate composite problem shown in Fig. 13a. The particulate composite is assumed to have properties similar to those of a heterogeneous solid propellant composed of very stiff, but compressible, Ammonium Perchlorate (AP) particles of various sizes ($\kappa_{AP} = 14.95$ GPa and $\mu_{AP} = 10.67$ GPa) embedded in a much more compliant quasi-incompressible binder ($\kappa_{Binder} = 12.5$ GPa and $\mu_{Binder} = 2.5$ MPa). The material response is modeled using the constitutive relations given in Section 2 and the modulus mismatch ratio μ^* for this problem is 3252. A pressure load of 2 MPa is applied on the top surface, while the bottom surface is free to move horizontally but restrained vertically. The point P is fixed horizontally as well to remove rigid body motions. All other surfaces are left traction-free. A structured finite element mesh independent of the circular particles is adopted (Fig. 13b).

Fig. 13b also shows the deformed shape of the idealized pack under the compressive load and emphasizes the heterogeneity of the deformation field, both in terms of the shape of the boundary, the deformed shapes of elements and the quasi-rigid rotation of the particles. The elements located between adjacent particles appear to experience substantial stretching in the direction perpendicular to the applied pressure, which points to the existence of tensile conditions in some regions of the pack. This particle-to-particle interaction is further illustrated in Fig. 14, which
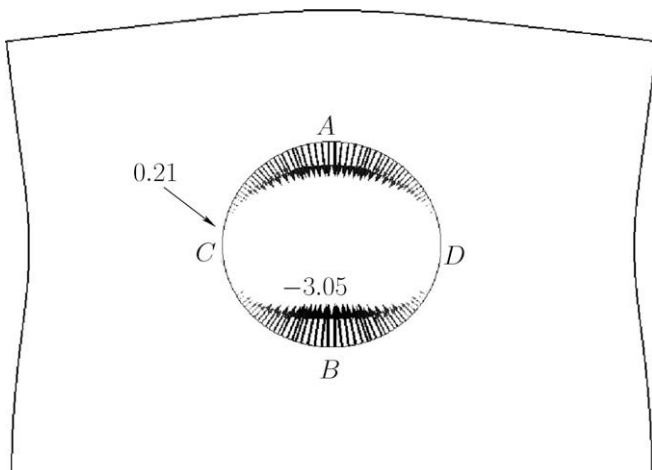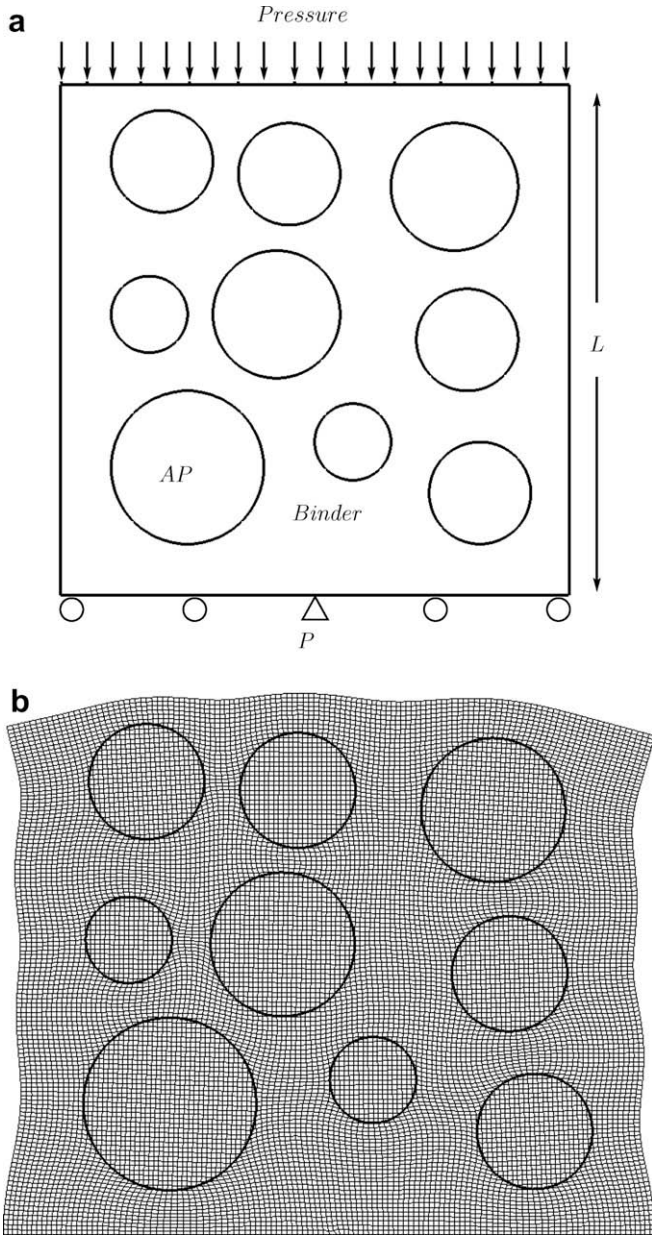
Fig. 13. (a) Schematic of the heterogeneous propellant pack made of Ammonium Perchlorate (AP) particles embedded in a polymeric binder; (b) deformed mesh showing the embedded AP/Binder interfaces, independent of element edges.

Fig. 14. Spatial distribution of pressure variable p in the heterogeneous propellant pack. Inset shows the normal tractions acting along the material interfaces at locations **A** and **B**.

Table 1
Residuals after each Newton–Raphson iteration of the non-linear solution step for the modeled heterogeneous solid propellant pack

Iter. No.	$\mathscr{R}_{\mathbf{u}}$	$\mathscr{R}_p$	$\mathscr{R}_\lambda$
1	1.8587E−01	2.2417E+00	6.1109E+00
2	9.8766E−03	9.2729E−02	2.1292E+00
3	2.8650E−04	2.7543E−03	1.4805E−01
4	4.5306E−07	1.4057E−06	1.2884E−03
5	2.2461E−12	9.5716E−13	1.6565E−07

Note that residuals for the volume field $\mathscr{R}_\theta$ attain machine precision immediately after the first iteration and are not listed.

presents the pressure field in the pack. While most of the domain is under compression ($p < 0$), some regions, such as those contained in boxes labeled **A** and **B** experience tension ($p > 0$). As shown in the inset, which present the spatial variation of the normal tractions acting along the AP/Binder interfaces, the inter-particle interaction leads to a state of tensile tractions along the boundary that might be a precursor to debonding. The effect is especially dominant when AP particles are close to each other. Despite the large gradients in the Lagrange multiplier field, the resulting normal tractions are generally smooth.

To indicate optimal rates of convergence of the Newton–Raphson scheme, the residuals (22) for the displacement $\mathbf{u}$, pressure p and Lagrange multiplier λ fields after each Newton–Raphson iteration are listed in Table 1. Note that, for the simple dilatational strain energy density U (5), the residuals for the volume unknown
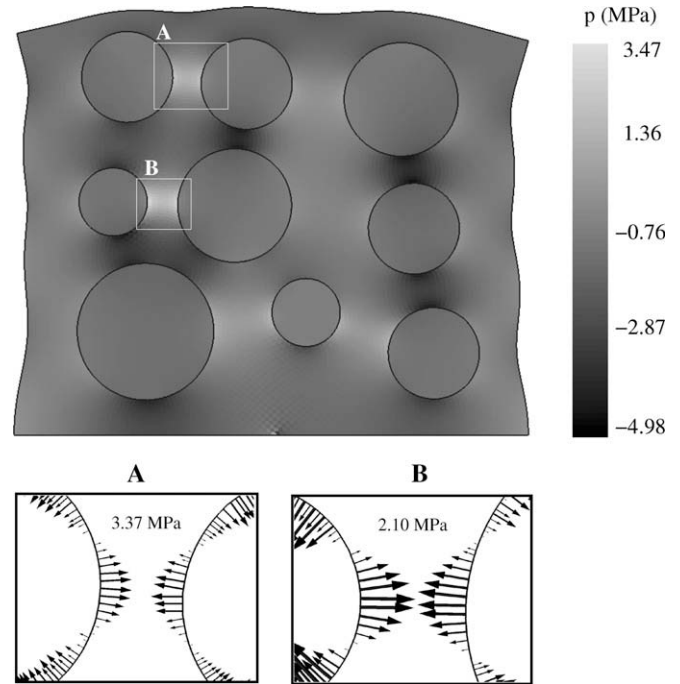
$\mathscr{R}_\theta$ (20) attain machine precision values immediately after the first iteration and are therefore not listed in Table 1.

6. Conclusions

The present work provides a numerical framework that combines the generalized finite element method with the classical mixed finite element method. Two formulations, based on a continuous and discontinuous deformation map, were derived and discretized for the motion of a bimaterial nearly incompressible hyperelastic solid. The two formulations were assessed numerically on the low-order Q_1/P_0 element, which is very popular in engineering practice, using a bimaterial patch test, and mesh convergence studies were carried out to evaluate the consistencies of the formulations. It was observed that both the continuous and discontinuous deformation maps yield convergent schemes for moderate modulus mismatches, while the continuous deformation map appears to be non-convergent for large mismatches. Finally, an idealized heterogeneous solid propellant pack is chosen as an example to demonstrate the capability and robustness of the discontinuous deformation map formulation.

Acknowledgements

Appendix A

Variations of the displacement approximation (17) required in the Euler–Lagrange equations (20) and (22) and the consistent tangent moduli (10) and (15) are derived as

$$
\delta\tilde{\boldsymbol{u}}(\boldsymbol{X}) = \underbrace{\sum_j^{N_J} \chi_j(\boldsymbol{X})\delta\hat{\boldsymbol{u}}_j}_{\delta\tilde{\boldsymbol{u}}^s(\boldsymbol{X})} + \sum_\alpha \underbrace{\sum_i^{N_I} \chi_i(\boldsymbol{X})\psi^\alpha \delta\hat{\boldsymbol{a}}_i^\alpha}_{\delta\tilde{\boldsymbol{u}}_\alpha^e(\boldsymbol{X})},
$$
$$
\Delta\tilde{\boldsymbol{u}}(\boldsymbol{X}) = \underbrace{\sum_j^{N_J} \chi_j(\boldsymbol{X})\Delta\hat{\boldsymbol{u}}_j}_{\Delta\tilde{\boldsymbol{u}}^s(\boldsymbol{X})} + \sum_\alpha \underbrace{\sum_i^{N_I} \chi_i(\boldsymbol{X})\psi^\alpha \Delta\hat{\boldsymbol{a}}_i^\alpha}_{\Delta\tilde{\boldsymbol{u}}_\alpha^e(\boldsymbol{X})},
\tag{A.1}
$$

with $\delta\tilde{\boldsymbol{u}}, \Delta\tilde{\boldsymbol{u}} \in H^1(\mathscr{B}_0^h)$, and $\mathscr{B}_0^h$ is the discretization of $\mathscr{B}_0$. Subsequently, variations of the deformation gradient $\tilde{\mathbf{F}}$ are approximated using (A.1) as

$$
\delta\tilde{\mathbf{F}} = \delta\tilde{\mathbf{F}}^s + \delta\tilde{\mathbf{F}}_\alpha^e \quad \text{with} \quad \delta\tilde{\mathbf{F}}^s = \nabla_{\boldsymbol{X}}\delta\tilde{\boldsymbol{u}}^s \quad \text{and} \quad \delta\tilde{\mathbf{F}}_\alpha^e = \nabla_{\boldsymbol{X}}\delta\tilde{\boldsymbol{u}}_\alpha^e,
$$
$$
\Delta\tilde{\mathbf{F}} = \Delta\tilde{\mathbf{F}}^s + \Delta\tilde{\mathbf{F}}_\alpha^e \quad \text{with} \quad \Delta\tilde{\mathbf{F}}^s = \nabla_{\boldsymbol{X}}\Delta\tilde{\boldsymbol{u}}^s \quad \text{and} \quad \Delta\tilde{\mathbf{F}}_\alpha^e = \nabla_{\boldsymbol{X}}\Delta\tilde{\boldsymbol{u}}_\alpha^e.
\tag{A.2}
$$

Similarly, variations of the pressure $\tilde{p}$ and volume $\tilde{\theta}$ approximations (19) are given by

$$
\delta\tilde{p}(\boldsymbol{X}) = \underbrace{\sum_j^{N_J^p} \chi_j^p(\boldsymbol{X})\delta\hat{p}_j}_{\delta p^s} + \sum_{\alpha^p} \underbrace{\sum_i^{N_I^p} \chi_i^p(\boldsymbol{X})\psi^{\alpha^p} \delta\hat{a}_i^{\alpha^p}}_{\delta p_{\alpha^p}^e},
$$
$$
\Delta\tilde{p}(\boldsymbol{X}) = \underbrace{\sum_j^{N_J^p} \chi_j^p(\boldsymbol{X})\Delta\hat{p}_j}_{\Delta p^s} + \sum_{\alpha^p} \underbrace{\sum_i^{N_I^p} \chi_i^p(\boldsymbol{X})\psi^{\alpha^p} \Delta\hat{a}_i^{\alpha^p}}_{\Delta p_{\alpha^p}^e}
\tag{A.3}
$$

and

$$
\delta\tilde{\theta}(\boldsymbol{X}) = \underbrace{\sum_j^{N_J^\theta} \chi_j^\theta(\boldsymbol{X})\delta\hat{\theta}_j}_{\delta\theta^s} + \sum_{\alpha^\theta} \underbrace{\sum_i^{N_I^\theta} \chi_i^\theta(\boldsymbol{X})\psi^{\alpha^\theta} \delta\hat{a}_i^{\alpha^\theta}}_{\delta\theta_{\alpha^\theta}^e},
$$
$$
\Delta\tilde{\theta}(\boldsymbol{X}) = \underbrace{\sum_j^{N_J^\theta} \chi_j^\theta(\boldsymbol{X})\Delta\hat{\theta}_j}_{\Delta\theta^s} + \sum_{\alpha^\theta} \underbrace{\sum_i^{N_I^\theta} \chi_i^\theta(\boldsymbol{X})\psi^{\alpha^\theta} \Delta\hat{a}_i^{\alpha^\theta}}_{\Delta\theta_{\alpha^\theta}^e}
\tag{A.4}
$$

with $\delta\tilde{p}, \Delta\tilde{p}, \delta\tilde{\theta}, \Delta\tilde{\theta} \in L_2(\mathscr{B}_0^h)$, while the variations of the Lagrange multiplier field $\tilde{\lambda}$, introduced in (21), are given by

$$
\delta\tilde{\lambda}(\boldsymbol{X}) = \sum_{j=1}^{N^\lambda} \chi_j^\lambda(\boldsymbol{X})\delta\hat{\lambda}_j, \quad \Delta\tilde{\lambda}(\boldsymbol{X}) = \sum_{j=1}^{N^\lambda} \chi_j^\lambda(\boldsymbol{X})\Delta\hat{\lambda}_j
\tag{A.5}
$$

with $\delta\tilde{\lambda}, \Delta\tilde{\lambda} \in H^{-\frac{1}{2}}(S_0^h)$, and S_0^h is the discretization of S_0. The approximated variations derived above are substituted in Eqs. (20) and (22) to establish static equilibrium.

For brevity, only the discretization of $\mathscr{R}_{\boldsymbol{u}^s}$ in (22) is shown below:

$$
\mathscr{R}_{\boldsymbol{u}^s} = \int_{\mathscr{B}_0^\pm} \hat{\mathbf{P}} : \nabla_{\boldsymbol{X}}\delta\boldsymbol{u}^s \, dV_0 + \int_{\mathscr{B}_0^\pm} \tilde{p}\tilde{J}\tilde{\mathbf{F}}^{-T} : \nabla_{\boldsymbol{X}}\delta\boldsymbol{u}^s \, dV_0
$$
$$
+ \int_{S_0} \tilde{\lambda} \cdot [\![\delta\tilde{\boldsymbol{u}}^s]\!] \, dS_0 = 0.
\tag{A.6}
$$

The consistent linearization of (A.6) using (15) and (11) yields

$$
D\mathscr{R}[\delta\boldsymbol{u}^s, \Delta\boldsymbol{u}^s] = \int_{\mathscr{B}_0^\pm} \nabla_{\boldsymbol{X}}\delta\boldsymbol{u}^s : \widehat{\mathscr{A}} : \nabla_{\boldsymbol{X}}\Delta\boldsymbol{u}^s \, dV_0
$$
$$
+ \int_{\mathscr{B}_0^\pm} \nabla_{\boldsymbol{X}}\delta\boldsymbol{u}^s : \tilde{p}\overline{\mathscr{A}} : \nabla_{\boldsymbol{X}}\Delta\boldsymbol{u}^s \, dV_0,
$$
$$
D\mathscr{R}[\delta\boldsymbol{u}^s, \Delta\boldsymbol{u}_\alpha^e] = \int_{\mathscr{B}_0^\pm} \nabla_{\boldsymbol{X}}\delta\boldsymbol{u}^s : \widehat{\mathscr{A}} : \nabla_{\boldsymbol{X}}\Delta\boldsymbol{u}_\alpha^e \, dV_0
$$
$$
+ \int_{\mathscr{B}_0^\pm} \nabla_{\boldsymbol{X}}\delta\boldsymbol{u}^s : \tilde{p}\overline{\mathscr{A}} : \nabla_{\boldsymbol{X}}\Delta\boldsymbol{u}_\alpha^e \, dV_0,
$$
$$
D\mathscr{R}[\delta\boldsymbol{u}^s, \Delta p^s] = \int_{\mathscr{B}_0^\pm} \nabla_{\boldsymbol{X}}\delta\boldsymbol{u}^s : \tilde{J}\tilde{\mathbf{F}}^{-T}\Delta p^s \, dV_0,
$$
$$
D\mathscr{R}[\delta\boldsymbol{u}^s, \Delta p_\alpha^e] = \int_{\mathscr{B}_0^\pm} \nabla_{\boldsymbol{X}}\delta\boldsymbol{u}^s : \tilde{J}\tilde{\mathbf{F}}^{-T}\Delta p_\alpha^e \, dV_0,
$$
$$
D\mathscr{R}[\delta\boldsymbol{u}^s, \Delta\theta^s] = 0,
$$
$$
D\mathscr{R}[\delta\boldsymbol{u}^s, \Delta\theta_\alpha^e] = 0,
$$
$$
D\mathscr{R}[\delta\boldsymbol{u}^s, \Delta\tilde{\lambda}] = \int_{S_0} [\![\delta\boldsymbol{u}^s]\!] \cdot \Delta\tilde{\lambda} \, dS_0.
\tag{A.7}
$$

References

[1] P. Areias, K. Matouš, Stabilized four-node tetrahedron with nonlocal pressure for modeling hyperelastic materials, Int. J. Numer. Methods Engrg., in press, doi:10.1002/nme.2357.

[2] P.M.A. Areias, T. Belytschko, A comment on the article, "a finite element method for simulation of strong and weak discontinuities in solid mechanics" by A. Hansbo and P. Hansbo [Computer Methods In Applied Mechanics Engineering 193 (2004) 3523-3540], Comput. Methods Appl. Mech. Engrg. 195 (9–12) (2006) 1275–1276.

[3] I. Babuška, Finite-element method with Lagrangian multipliers, Numer. Math. 20 (3) (1973) 179–192.

[4] I. Babuška, G.N. Gatica, On the mixed finite element method with Lagrange multipliers, Numer. Methods Partial Diff. Equat. 19 (2) (2003) 192–210.

[5] I. Babuška, J.M. Melenk, The partition of unity method, Int. J. Numer. Methods Engrg. 40 (4) (1997) 727–758.

[6] T. Belytschko, T. Black, Elastic crack growth in finite elements with minimal remeshing, Int. J. Numer. Methods Engrg. 45 (5) (1999) 601–620.

[7] T. Belytschko, N. Moës, S. Usui, C. Parimi, Arbitrary discontinuities in finite elements, Int. J. Numer. Methods Engrg. 50 (4) (2001) 993–1013.

[8] F. Brezzi, M. Fortin, Mixed and Hybrid Finite Element Methods, Springer, 1991.

[9] D. Chapelle, K.J. Bathe, The inf–sup test, Comput. Struct. 47 (4–5) (1993) 537–545.

[10] D.L. Chopp, N. Sukumar, Fatigue crack propagation of multiple coplanar cracks with the coupled extended finite element/fast marching method, Int. J. Engrg. Sci. 41 (8) (2003) 845–869.

[11] B. Collins, F. Maggi, K. Matous, T. Jackson, J. Buckmaster, Using tomography to characterize heterogeneous solid propellants, in: 46th AIAA Aerospace Sciences Meeting and Exhibit, 7–10 January 2008, Reno, Nevada, number 2008-0941, 2008.

[12] J. Dolbow, N. Moës, T. Belytschko, Discontinuous enrichment in finite elements with a partition of unity method, Finite Elem. Anal. Des. 36 (3–4) (2000) 235–260.

[13] J.E. Dolbow, A. Devan, Enrichment of enhanced assumed strain approximations for representing strong discontinuities: addressing volumetric incompressibility and the discontinuous patch test, Int. J. Numer. Methods Engrg. 59 (1) (2004) 47–67.

[14] C.A. Duarte, I. Babuška, J.T. Oden, Generalized finite element methods for three-dimensional structural mechanics problems, Comput. Struct. 77 (2) (2000) 215–232.

[15] C.A. Duarte, O.N. Hamzeh, T.J. Liszka, W.W. Tworzydlo, A generalized finite element method for the simulation of three-dimensional dynamic crack propagation, Comput. Methods Appl. Mech. Engrg. 190 (15–17) (2001) 2227–2262.

[16] C.A. Duarte, J.T. Oden, An h-p adaptive method using clouds, Comput. Methods Appl. Mech. Engrg. 39 (1–4) (1996) 237–262.

[17] C.A. Duarte, L.G. Reno, A. Simone, High-order generalized FEM for through-the-thickness branched cracks, Int. J. Numer. Methods Engrg. 72 (3) (2007) 325–351.

[18] A. Hansbo, P. Hansbo, A finite element method for the simulation of strong and weak discontinuities in solid mechanics, Comput. Methods Appl. Mech. Engrg. 193 (33–35) (2004) 3523–3540.

[19] T. Hettich, E. Ramm, Interface material failure modeled by the extended finite-element method and level sets, Comput. Methods Appl. Mech. Engrg. 195 (37–40) (2006) 4753–4767.

[20] T.J.R. Hughes, L.P. Franca, M. Balestra, A new finite-element formulation for computational fluid-dynamics: V. Circumventing the Babuška–Brezzi condition – a stable Petrov–Galerkin formulation of the stokes problem

accommodating equal-order interpolations, Comput. Methods Appl. Mech. Engrg. 59 (1) (1986) 85–99.

[21] T.Y. Kim, J. Dolbow, T. Laursen, A mortared finite element method for frictional contact on arbitrary interfaces, Comput. Mech. 39 (3) (2007) 223–235.

[22] S. Kochevets, J. Buckmaster, T.L. Jackson, A. Hegab, Random propellant packs and the flames they support, J. Propulsion Power 17 (4) (2001) 883–891.

[23] G. Legrain, N. Moës, E. Verron, Stress analysis around crack tips in finite strain problems using the extended finite element method, Int. J. Numer. Methods Engrg. 63 (2) (2005) 290–314.

[24] A. Masud, K. Xia, A stabilized mixed finite element method for nearly incompressible elasticity, J. Appl. Mech. 72 (5) (2005) 711–720.

[25] K. Matouš, P.H. Geubelle, Finite element formulation for modeling particle debonding in reinforced elastomers subjected to finite deformations, Comput. Methods Appl. Mech. Engrg. 196 (1–3) (2006) 620–633.

[26] J. Mergheim, E. Kuhl, P. Steinmann, A finite element method for the computational modelling of cohesive cracks, Int. J. Numer. Methods Engrg. 63 (2) (2005) 276–289.

[27] N. Moës, M. Cloirec, P. Cartraud, J.F. Remacle, A computational approach to handle complex microstructure geometries, Comput. Methods Appl. Mech. Engrg. 192 (28–30) (2003) 3163–3177.

[28] N. Moës, J. Dolbow, T. Belytschko, A finite element method for crack growth without remeshing, Int. J. Numer. Methods Engrg. 46 (1) (1999) 131–150.

[29] N. Moës, J. Dolbow, T. Belytschko, A finite element method for crack growth without remeshing, Int. J. Numer. Methods Engrg. 46 (1) (1999) 131–150.

[30] S. Osher, J.A. Sethian, Fronts propagating with curvature-dependent speed – algorithms based on Hamilton–Jacobi formulations, J. Comput. Phys. 79 (1) (1988) 12–49.

[31] B. Ramesh, A.M. Maniatty, Stabilized finite element formulation for elasticplastic finite deformations, Comput. Methods Appl. Mech. Engrg. 194 (6-8) (2005) 775–800.

[32] J.C. Simo, R.L. Taylor, K.S. Pister, Variational and projection methods for the volume constraint in finite deformation elasto-plasticity, Comput. Methods Appl. Mech. Engrg. 51 (1–3) (1985) 177–208.

[33] A. Simone, C.A. Duarte, E. Van der Giessen, A generalized finite element method for polycrystals with discontinuous grain boundaries, Int. J. Numer. Methods Engrg. 67 (8) (2006) 1122–1145.

[34] M. Stolarska, D.L. Chopp, N. Moës, T. Belytschko, Modelling crack growth by level sets in the extended finite element method, Int. J. Numer. Methods Engrg. 51 (8) (2001) 943–960.

[35] T. Strouboulis, K. Copps, I. Babuška, The generalized finite element method, Comput. Methods Appl. Mech. Engrg. 190 (32–33) (2001) 4081–4193.

[36] N. Sukumar, D.L. Chopp, N. Moës, T. Belytschko, Modeling holes and inclusions by level sets in the extended finite-element method, Comput. Methods Appl. Mech. Engrg. 190 (46–47) (2001) 6183–6200.

[37] N. Sukumar, D.L. Chopp, B. Moran, Extended finite element method and fast marching method for three-dimensional fatigue crack propagation, Engrg. Fracture Mech. 70 (1) (2003) 29–48.

[38] B.L. Vaughan, B.G. Smith, D.L. Chopp, A comparison of the extended finite element method with the immersed interface method for elliptic equations with discontinuous coefficients and singular sources, Commun. Appl. Math. Comput. Sci. 1 (1) (2006) 07–228.